Journal of Electromyography and Kinesiology 86 (2026) 103103

Contents lists available at ScienceDirect

Journal of Electromyography and Kinesiology

journal homepage: www.elsevier.com/locate/jelekin

# The influence of muscle shapes on HDsEMG decomposition yield and accuracy

Andra Oltmann [a,*], Jan Graßhoff [a], Tobias Knopp [a,b,c], Philipp Rostalski [a,d]

[a] Fraunhofer IMTE, Fraunhofer Research Institution for Individualized and Cell-Based Medical Engineering, Lübeck, Germany
[b] Section for Biomedical Imaging, University Medical Center Hamburg-Eppendorf, Hamburg, Germany
[c] Institute for Biomedical Imaging, Hamburg University of Technology, Hamburg, Germany
[d] Institute for Electrical Engineering in Medicine, University of Lübeck, Lübeck, Germany

ARTICLE INFO

*Keywords:*
High-density surface electromyography
Surface electromyography decomposition
Muscle modeling
Numerical computer simulation
Biceps brachii

ABSTRACT

The application of high-density surface electromyography in conjunction with decomposition algorithms has enabled decoding of motor unit (MU) firings. In developing such algorithms, model-based simulation is an established means to assess yield and accuracy. In this work, we therefore investigate how the simulated muscle shape impacts the decomposition performance.

To this end, an arm model with an anatomical biceps brachii shape was developed, and its plausibility in representing MU action potential waveforms was verified with decomposition of experimental, submaximal ramp contractions. From this anatomical muscle shape model, two simplified shapes were derived. In a simulation study, comparable fiber pathways and MU properties were used in anatomical and simplified muscle shape models, and a blind source separation-based decomposition was performed. The results were evaluated with respect to the number of identified MUs and their rate of agreement (RoA).

Across all models, MUs with the highest energy contribution were identified. For the two simplified shapes, statistically significantly more MUs ($p < 0.05$) were decomposed due to changed electrode-fiber distances, while the RoA remained consistently high above $94.63 \pm 12.16$ % indicating reliable MU property extraction with all three models. The results emphasize the benefit of anatomically accurate muscle shape models since small simplifications can affect decomposition yield.

## 1. Introduction

Surface electromyography (sEMG) is a non-invasive method for measuring potentials generated by the electrical activity of muscle fibers during muscle contractions. Electrodes on the skin surface sample the spatial and temporal superposition of motor unit action potentials (MUAPs) from active motor units (MUs) each comprising the potentials generated by up to thousands of individual fibers [Merletti and Farina, 2016, section 1-2]. While monopolar or bipolar electrode arrangements can be considered to derive a global muscle activity measure [Farina et al., 2004a], high-density sEMG (HDsEMG) enables the non-invasive decoding of MU firings and properties [Del Vecchio et al., 2020]. Through the arrangement of a large number of small-diameter electrodes in a closely spaced grid, HDsEMG recordings provide a sampling of MUAPs at high spatial resolution, which supports recognition and separation of MUs from different parts of the muscle by means of blind source separation [Del Vecchio et al., 2020].

In the development of HDsEMG decomposition algorithms, modeling has become an established method to generate ground truth data for performance validation [Farina et al., 2014] and has frequently been used [Avrillon et al., 2024; Grison et al., 2025; Mendez Guerra et al., 2024]. In all models used in these studies sEMG signals are represented as a convolutive mixture of active MU discharge series and their corresponding MUAP templates. While in most of these publications the same type of models is used for simulating MU recruitment and firing behavior, two approaches can be distinguished for the calculation of MUAP templates. On the one side analytical models have been used to simulate the potential field propagation in simplified volume conductor shapes with few tissue layers and parallel extending muscle fibers [Farina et al., 2004b; Farina and Merletti, 2001]. On the other side numerical models use finite element methods (FEM) to integrate realistic muscle anatomies and tissue inhomogeneities derived from three-

* Corresponding author.
*E-mail address:* andra.oltmann@imte.fraunhofer.de (A. Oltmann).

https://doi.org/10.1016/j.jelekin.2025.103103
Received 26 September 2025; Received in revised form 3 December 2025; Accepted 17 December 2025
Available online 18 December 2025

dimensional image data [Maksymenko et al., 2023; Pereira Botelho et al., 2019]. Whereas analytical models are characterized by faster calculation times, anatomically derived FEM models are substantially more complex, require extensive computational resources and have therefore rarely been used for modeling MUAP field propagation to date. Recently, an implementation of a more computationally efficient procedure has been proposed by Maksymenko et al., 2023, in order to foster a more viable application of FEM models for analyzing sEMG data.

Our investigation started with a seemingly simple but unresolved question: Which model should be used to simulate HDsEMG data? Is it worth adopting an anatomically accurate, numerical muscle model, or would a simplified, cylindrical model suffice? Intuition suggests that overly simplistic geometries may lose key aspects of volume conduction and thus affect decomposition algorithms. Experimental experience supports this concern: HDsEMG decomposition performance depends on factors such as muscle type and subcutaneous thickness [Del Vecchio et al., 2020]. Therefore, the choice of simulation model likely plays a decisive role in evaluating new algorithms. Despite its importance, the impact of model choice has not yet been studied.

Thus, we aim to investigate the impact of the modeled muscle shape on HDsEMG decomposition yield and accuracy. To this end, we implemented an anatomically derived arm model incorporating biceps brachii muscle geometries with varying degrees of simplification. Before analyzing the impact of the modeled muscle shapes on the performance of a blind source separation-based decomposition algorithm in a simulation study, we verified the plausibility of the anatomical model in representing MUAP waveforms using experimental HDsEMG measurements acquired during isometric submaximal ramp contractions.

## 2. Methods

In this section, we will first introduce the different muscle shape models and explain the simulation study that was conducted. This will be followed by a description of the experimental measurements used to verify the anatomical muscle model. Finally, we will explain our data analysis and statistical evaluation.

### 2.1. Mathematical model

#### 2.1.1. Model overview

Building upon earlier models from the literature, we derived a biceps brachii model and employed it to generate HDsEMG and muscle force signals. The model comprises a pipeline of five sequential calculation steps, i.e., the discretization of the volume conductor into a tetrahedral volume mesh (1), the generation of realistic muscle fiber pathways (2), the organization of the underlying motor unit pool (3), the numerical solution of the potential field propagation with MUAP determination (4), and the calculation of MU force twitches (5). In this work, we adapt established mathematical formulations for neuromuscular aspects, such as MU pool properties, and add geometrical models for the muscle shape. The subsequent sections delineate the volume conductor implementation with different muscle shapes, fiber pathway generation, geometrical MU pool organization and simulation experiments. For the sake of reproducibility, an extended description of the model components (1)-(5) and an overview of selected model parameters are given in the *Supplementary Material*.

#### 2.1.2. Volume conductor and muscle shape geometries

An anatomically derived volume conductor model of the arm was developed to analyze muscle shape simplifications with the biceps brachii as primary muscle of interest. The model consisted of the trunk, ulna, radius, humerus, scapula, and biceps brachii components imported from *BodyParts3D* [Mitsuhashi et al., 2009]. We added a subcutaneous fat and skin tissue layer with a uniform thickness of 3 mm and 1.5 mm, respectively. To simulate HDsEMG signals, we implemented an electrode grid with 64 electrodes located on the skin above the muscle belly. Circular electrodes with a diameter of 4 mm were arranged with an inter-electrode distance (IED) of 8.75 mm in 6 columns and 11 rows. A circular reference electrode was attached to the lateral elbow joint. An overview of the finalized anatomical volume conductor is depicted in Fig. 1A.

We implemented three muscle geometries with varying degrees of simplification. The anatomical geometry was constructed from the long and short head biceps brachii components of *BodyParts3D* [Mitsuhashi et al., 2009]. The two simplified muscle geometries were approximated from the anatomical cross-sections. For the first simplified muscle geometry (*fusiform* muscle shape) we implemented semi-cylindrical cross-sections that tapered along the longitudinal muscle axis. For the second simplified geometry (*cylindrical* muscle shape) the semi-cylindrical cross-section remained constant over the entire muscle length. For both the fusiform and the cylindrical geometry, we optimized the muscle cross-sections to maximize area overlap with the anatomical cross-sections. Selected anatomical cross-sections and their fusiform and cylindrical approximations are visualized in Fig. 1B.

In order to optimally integrate the simplified geometries into the anatomical volume conductor, we manually adapted the muscle–tendon-junctions accordingly using SOLIDWORKS 2023 (Dassault Systemes SolidWorks Corporation, Waltham, USA). All three volume conductors were discretized with tetrahedral volume elements of comparable size. In COMSOL Multiphysics v6.3 (COMSOL AB, Stockholm, Sweden), the FEM meshes with the anatomical, fusiform and cylindrical muscle shape consisted of 5259559, 5113580 and 5551216 elements, respectively. Convergence studies were performed to ensure numerical adequacy.

#### 2.1.3. Fiber pathways

Ensuring that the properties across the three models are as consistent as possible is crucial for isolating the effect of muscle shape on HDsEMG decomposition. This implies the need for consistent fiber-electrode distances, which was ensured by mapping fiber base points during the fiber pathway generation process.

Firstly, we homogeneously distributed 208645 muscle fiber base points $(x_f, y_f)$ inside the largest muscle cross-section of the anatomical muscle shape model according to Duchateau and Enoka, 2022 (see Fig. 2A). For the two simplified muscle geometries, the fiber base point distribution was obtained by performing a geometry mapping. To this end, we performed a shape registration between the anatomical cross-section and the simplified ones using optimal transport. The registration was based on two point sets $A = \{A_1, A_2, \cdots, A_o\}$ and $B = \{B_1, B_2, \cdots, B_p\}$ with $o \approx p$. The point sets consisted of points which were equidistantly distributed over a rectangular grid inside the anatomical and simplified shape, respectively. From these point sets, we formed a cost matrix $C$ whose entries $c_{rs}$ are the squared Euclidean distance between $A_r$ and $B_s$. In order to register the two point sets, a transport matrix $\gamma$ was determined by minimizing the optimization problem [Villani, 2008]

$$\min_{\gamma} \sum_{r=1}^{o} \sum_{s=1}^{p} \gamma_{rs} c_{rs} \tag{1}$$

with the constraints

$$\sum_{s=1}^{p} \gamma_{rs} = a_r = \frac{1}{o}, \quad \sum_{r=1}^{o} \gamma_{rs} = b_s = \frac{1}{p}, \text{ and } \gamma_{rs} \geq 0 \ \forall r, s. \tag{2}$$

Here, the transportation matrix $\gamma$ describes how the point masses are transformed from the source point set $A$ to the target point set $B$. Using this matrix, we derived displacements in $x$ and $y$ direction for all equidistant points in the point set $A$. Subsequently, the muscle fiber base points $(x_f, y_f)$ inside the anatomical muscle shape were translated into the simplified muscle cross-sections through interpolation of the calculated displacements.

Secondly, we calculated the muscle fiber trajectories corresponding

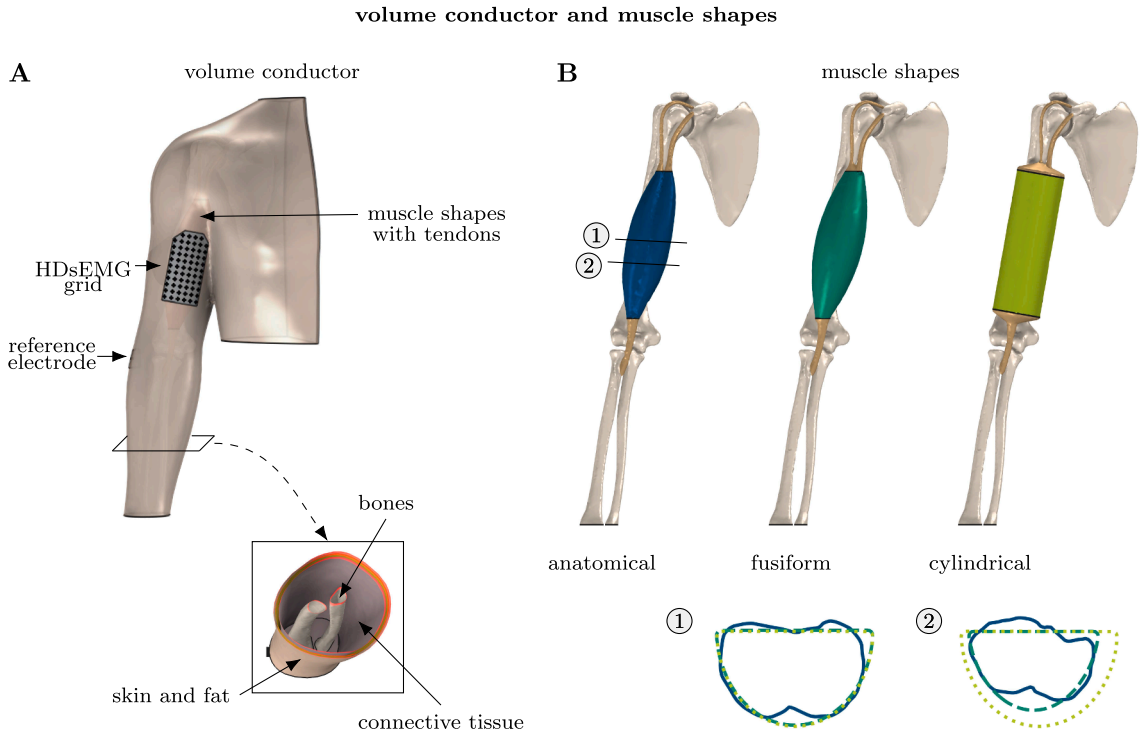


**Fig. 1.** Panel A gives an overview of the implemented volume conductor model. The basic geometry with the high-density surface electromyography (HDsEMG) grid and a cross-sectional view of the forearm are depicted. Panel B visualizes the three implemented muscle shapes with the muscle cross-sections at both the muscle belly (1) and towards the distal end of the muscle (2).

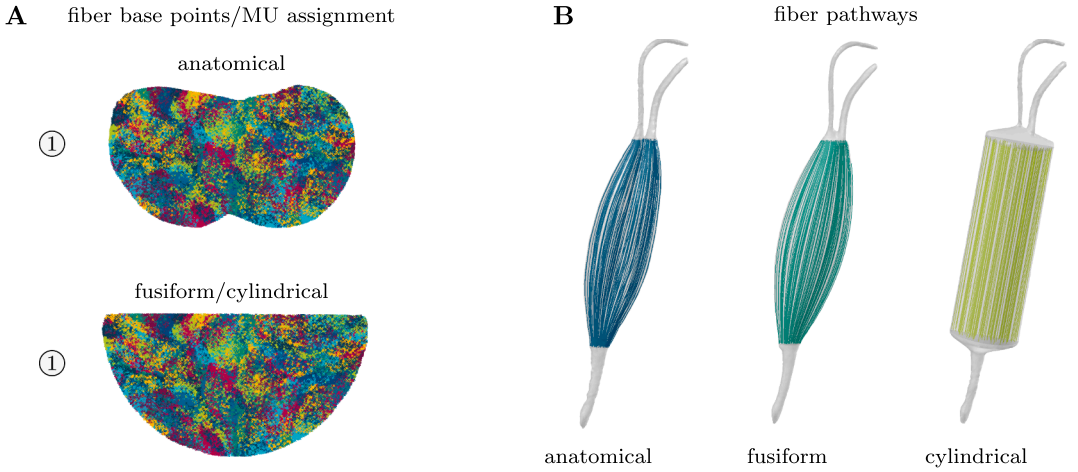


**Fig. 2.** Panel A depicts muscle fiber base points at the muscle belly (1) and an exemplary assignment to motor units, which are indicated by different colors. Fiber pathways generated from an excerpt of muscle fiber base points are illustrated in panel B for all three muscle domains.

to the base points from streamlines of a stationary Laplacian potential flow through the muscle geometry [Choi and Blemker, 2013]. To this end, the Laplace equation, $\Delta u(\boldsymbol{x}) = 0$, with scalar potential $u(\boldsymbol{x})$ was solved inside the muscle domains and the normalized vector fields $\widetilde{\boldsymbol{v}}(\boldsymbol{x}) = \frac{-\nabla u(\boldsymbol{x})}{|-\nabla u(\boldsymbol{x})|}$ were numerically calculated using COMSOL Multiphysics v6.3. To obtain a unique solution, we applied Neumann and Dirichlet boundary conditions: $\boldsymbol{n}(\boldsymbol{x})\cdot\nabla u(\boldsymbol{x}) = 0$ was assumed for the boundary in parallel to the skin surface, a unit potential was used at the distal muscle–tendon-junction, and a ground condition was imposed at the proximal muscle–tendon-junction. Based on the resulting three-dimensional normalized vector field, fiber pathways were estimated as streamlines by numerically integrating the vector field in both directions from the fiber base points. An excerpt of calculated pathways is depicted in Fig. 2B for all three muscle shapes.

### 2.1.4. MU pool

Besides the three-dimensional fiber pathways, the functional and geometrical arrangement of MUs also affect MUAP waveforms. Therefore, we mapped corresponding fibers to the same MU across all muscle shapes. For functional organization, we implemented a size-principle MU pool and firing rate model according to Petersen and Rostalski, 2019, with parameters adapted to the biceps brachii (see *Supplementary*

*Material*), from which we calculated MU discharge series.

In each simulation, we sampled the number of MUs $n$ from a normal distribution $n \sim \mathcal{N}(312, 51)$, which goes back to the data analyzed by Duchateau and Enoka, 2022. MU centers were then placed uniformly within the largest anatomical cross-section, independent of MU size. Following Maksymenko et al., 2023, we assigned muscle fibers to MUs if they were within the circular MU area. When a fiber was in more than one MU area, it was assigned to the MU that was still missing the greatest number of fibers to reach its expected size. An exemplary MU assignment to muscle fibers is depicted in Fig. 2A. Changing the random seed varied not only the number of MUs and their position in the cross section, but also physiological properties and the generation of discharge series.

#### 2.1.5. MUAP waveforms and sEMG interference signals

Each MU comprises a motor neuron and the muscle fibers it innervates. At each motor neuron, discharge current source action potentials are generated, which propagate along the muscle fibers and cause extracellular potential distributions in the volume conductor [Merletti and Farina, 2016, section 1-2]. The extracellular potential distribution $\phi(\boldsymbol{x})$ can be calculated with Poisson's equation [Merletti and Farina, 2016, section 8],

$$\nabla\cdot(\boldsymbol{\sigma}(\boldsymbol{x})\nabla\phi(\boldsymbol{x})) = -I,\ \boldsymbol{x} \in \boldsymbol{\Omega} \tag{3}$$

where $\boldsymbol{\sigma}(\boldsymbol{x})$ is a conductivity tensor and $I$ is the current density source. We used boundary conditions,

$$\boldsymbol{n}(\boldsymbol{x})\cdot(\boldsymbol{\sigma}(\boldsymbol{x})\nabla\phi(\boldsymbol{x})) = 0,\ \boldsymbol{x} \in \partial\boldsymbol{\Omega}_{\mathbf{air}},$$

$$\phi(\boldsymbol{x}) = 0,\ \boldsymbol{x} \in \partial\boldsymbol{\Omega}_{\mathbf{trunk}}, \tag{4}$$

where $\boldsymbol{\Omega}$ denotes the volume conductor domain with boundary $\partial\boldsymbol{\Omega}_{\mathbf{air}}$ from skin to air, and $\partial\boldsymbol{\Omega}_{\mathbf{trunk}}$ is the boundary where the domain is truncated, $\boldsymbol{n}(\boldsymbol{x})$ is the normal vector to $\partial\boldsymbol{\Omega}$, and $\boldsymbol{x}$ is a vector of the spatial coordinates $(x, y, z)$. The $\mathrm{MUAP}_{ji}$ was obtained by summing extracellular potentials of fibers from MU $i$ on a specific electrode channel $j$.

The equation system ((3)-(4)) can numerically be solved by discretizing the domain into finite elements and solving a corresponding linear system. Since calculating the potential distribution for each muscle fiber is computational demanding, we applied the principle of reciprocity proposed by Pereira Botelho et al., 2019. Instead of simulating the current density of each muscle fiber, this approach injects currents at the electrodes, which significantly reduced the number of linear equations to be solved. Applied conductivity values are listed in the *Supplementary Material*. Muscle anisotropy was modeled with a ratio of 4.4 between longitudinal and transverse fiber direction while aligning the conductivity tensor with the curved fiber direction fields obtained during pathway generation. All numerical calculations were performed with COMSOL Multiphysics v6.3.

The sEMG interference signal $\mathrm{sEMG}_j[k]$ of an electrode channel $j$ can be expressed as convolutive mixture of $n$ sources (MUs) with corresponding MUAP templates [Farina and Holobar, 2016]:

$$\mathrm{sEMG}_j[k] = \sum_{l=0}^{L-1}\sum_{i=1}^{n}\mathrm{MUAP}_{ji}[l]s_i[k-l] \text{ with } \mathrm{j} = 1,\cdots,64 \text{ and } k = 0,\cdots,D_R-1. \tag{5}$$

Here, $k$ is the discrete time, $D_R$ is the simulation duration in samples, $L$ is the action potential duration in samples, $\mathrm{MUAP}_{ji}[l]$ denotes the action potential of the $i$th MU as recorded at channel $j$, and $s_i[k]$ is the spike train of MU $i$ with spikes at discharge times. In all three models we used the same random seeds, leading to identical spike trains in corresponding MUs.

#### 2.1.6. Simulation experiments

Using 16 stochastic seeds we simulated monopolar MUAP waveforms and generated spike trains of submaximal ramp contraction, from which we calculated monopolar HDsEMG signals sampled at 2048 Hz. For each stochastic seed, eight submaximal ramp contractions with four different target forces (15%, 30%, 50%, and 70% maximum voluntary contraction force (MVCF), two repetitions each) were implemented. The isometric force was kept constant for 30 s (at 15% and 30% MVCF) and 10 s (at 50% and 70% MVCF), respectively. We simulated linear ramps with slopes of 5% MVCF/s (15% and 30% MVCF) and 10% MVCF/s (50% and 70% MVCF). Zero-mean white Gaussian noise with a standard deviation of 10 μV was added to each of the 64 sEMG channels, which is a level that is comparable to values observed in the experimental measurements described in the following section. The same noise pattern was applied to corresponding channels and stochastic seeds of different muscle shape simulations, respectively.

### 2.2. Experimental measurements

To assess the plausibility of the proposed anatomical biceps brachii volume conductor model in reproducing experimental MUAP waveforms, we acquired HDsEMG and force data during isometric, submaximal ramp contractions. Data was obtained from a total of 16 adult participants with exclusion criteria being body-mass-index over 50 kg/m$^2$, neuromuscular diseases and central nervous system diseases. The local ethics committee (University of Lübeck, Lübeck, Germany, reference no. 2023-480_3, September 2024) approved the study protocol and all subjects declared written informed consent.

A detailed description of the performed study protocol is described in the *Supplementary Material*. Briefly, the study was conducted in one session comprising maximum voluntary contractions, a familiarization with predefined target forces, and the recording of submaximal ramp contractions with the same eight force profiles as in the simulation experiments.

The muscle force of the dominant arm generated during submaximal ramp contractions was assessed with a load cell (S-Type Load Cell – 100 kg, Phidgets Inc., Calgary, Canada), which was connected to the wrist by a cuff. Participants were seated in an upright position with the upper arm in parallel to the torso, an elbow joint angle of 135° and the forearm in supination. The force signal was amplified by a micro-controller (ESP32, Espressif Systems, Shanghai, China) and forwarded to the analog input of the sEMG recording device for synchronous recording at 2048 Hz.

In order to ensure maximum comparability with the simulations, electrodes of the same size and with the same IED were used. In addition, the HDsEMG grid had the same topology and was applied in a comparable position. Before recording HDsEMG signals the participants' skin was shaved, cleaned and slightly abraded. The biceps brachii was identified through palpation. An adhesive grid with 64 electrodes (6 columns × 11 rows, diameter: 4 mm, IED: 8.75 mm) was positioned above the muscle belly oriented in direction of the muscle fibers. To ensure electrode–skin contact, conductive gel (ELECTRO-GEL, E9, Electro-Cap International, Inc., Eaton, USA) was applied. A reference electrode and a technical ground electrode (Kendall H124SG, CardinalHealth, Dublin, Ireland) were positioned above the lateral and medial part of the elbow joint, respectively. HDsEMG signals were recorded in monopolar mode with a sampling rate of 2048 Hz using the 24-bit multi-channel amplifier TMSi SAGA 64+ (TMSi, Oldenzaal, Netherlands). A schematic representation of the experimental measurement setup is shown in Fig. 3A.

### 2.3. Data analysis

#### 2.3.1. High-density surface electromyography signal decomposition

HDsEMG signals were bandpass filtered with cutoff frequencies of 20–500 Hz, using a second-order Butterworth filter implemented with the two-pass zero-phase technique. Additionally, powerline interference was removed.

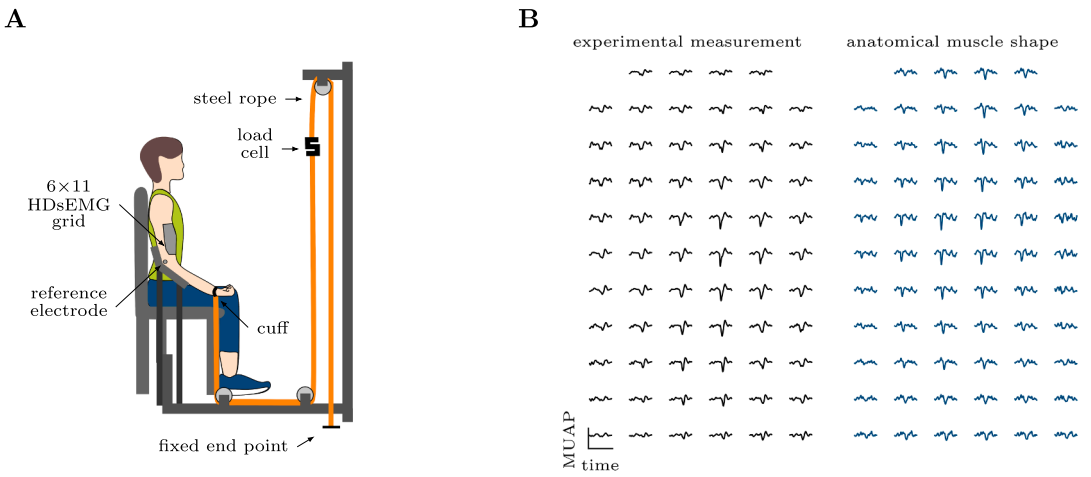


**Fig. 3.** Panel A illustrates the experimental measurement setup for HDsEMG signal acquisition from which motor unit action potential (MUAP) waveforms were decomposed. Panel B exemplary visualizes two-dimensional MUAP waveforms calculated with spike-triggered averaging of motor units (MUs) which were decomposed from experimental measurement (black – m) and anatomical simulation trials (anatomical – a – darkblue) of a submaximal ramp contraction at 50% maximum voluntary contraction force (MVCF).

We performed MU decomposition of simulated and measured HDsEMG signals with *MUEdit* [Avrillon et al., 2024]. *MUEdit* is an open-source software that identifies MU discharge times from HDsEMG signals acquired with multi-channel systems. Through the application of source separation algorithms, i.e., fast independent component analysis, the discharge times of particular MUs are estimated from iteratively optimized separation vectors. We performed MU decomposition in *MUEdit* using the *logcosh* contrast function. Only MUs with a coefficient of variation of their inter-spike intervals lower than 2 and a silhouette measure (SIL) higher than 0.9 were automatically identified. The SIL quantifies the degree of separability between identified MUs and noise [Negro et al., 2016]. Afterwards an investigator manually analyzed the decomposed spike trains. This analysis included visual inspection of the automatically identified discharge times to check for falsely identified discharges or missed ones. In an iterative process, separation vectors were recalculated, and discharge timings were updated. We only retained MUs with a SIL higher than 0.9 and a coefficient of variation lower than 0.5.

### 2.3.2. Comparison of MUAP waveforms for plausibility checking

To check whether the anatomical muscle shape model is able to reproduce plausible physiological characteristics, two-dimensional MUAP waveforms were calculated for decomposed MUs (SIL $>$ 0.93) of experimental measurements and the anatomical simulations. To avoid duplicates only the trial with the highest amount of decomposed MUs was considered for each target force. Assuming that the MUAP shape of individual MUs are relatively constant during isometric contractions, we applied spike-triggered averaging (STA) with a window size of 50 ms to the first 50 spikes to obtain the surface MUAP distribution at all electrodes of the HDsEMG grid [Del Vecchio et al., 2020]. An exemplary excerpt of two-dimensional MUAP waveforms obtained with STA for experimental measurements and the anatomical muscle shape model is depicted in Fig. 3B.

To assess spatial variations of power and shape, we calculated the peak-to-peak (PTP) amplitude ($\mathrm{MUAP}_{\mathrm{ptp}_j}$) and mean frequency ($\mathrm{MUAP}_{\mathrm{MNF}_j}$) of MUAP waveforms for each electrode channel. For better comparability between experimental and modeled data, both metrics were reported as 2D maps, which for each MUAP were centered on the electrode with the maximal PTP. These centered maps were then averaged for further analysis.

### 2.3.3. MU identification and validation in muscle shape simulations

For each muscle shape model, we investigated the number of identified MUs per trial. To validate the MU decomposition results we determined a corresponding simulated spike train for each decomposed discharge series. The MU whose spike train maximized the discrete cross-correlation with the decomposed spike train was considered as the matching MU. A common metric to evaluate decomposition accuracy of an identified MU is the rate of agreement with the matched MU [Negro et al., 2016]

$$\mathrm{RoA}_i = \frac{\epsilon_i}{\epsilon_i + D_i + E_i}, \tag{6}$$

where $\epsilon_i$ is the number of spikes that were both identified with *MUEdit* and present in the ground truth, $D_i$ is the number of spikes only identified with the decomposition algorithm, and $E_i$ is the number of spikes only present in the matched MU. We applied a tolerance of $\pm$ 0.98 ms for matching discharge events, which corresponds to two sampling points and is substantially lower than the typical MUAP duration.

MUs are typically considered identifiable if their MUAP contribute strongly to sEMG signal energy [Avrillon et al., 2024; Farina and Holobar, 2016]. This is the case, on the one hand, for larger MUs comprising several muscle fibers, and, on the other hand, for MUs closely located to the electrodes. To examine whether muscle shape has an influence on MU detection, we compared the positions of detected MUs, and their sizes relative to the largest unit in the pool ($\mathrm{MU}_{\mathrm{size}}$).

## 2.4. Statistics

To compare the identified MUAPs in the measurement data with those from the anatomical model, independent t-tests were performed for $\mathrm{MUAP}_{\mathrm{ptp}_{\mathrm{max}}}$ and $\mathrm{MUAP}_{\mathrm{MNF}_{\mathrm{max}}}$, calculated for the electrode channel with the highest MUAP PTP amplitude.

To evaluate the impact of the modeled muscle shape on the performance of the decomposition algorithm, matched paired t-tests were used to compare the difference in identified MUs per trial with results grouped into target forces. Furthermore, independent t-tests were used to assess differences in RoA and relative $\mathrm{MU}_{\mathrm{size}}$. For all tests, statistical significance was set at $p < 0.05$, with Bonferroni-Holm correction for multiple comparisons between subgroups [Armstrong, 2014]. Data are reported as mean $\pm$ standard deviation.

## 3. Results

### 3.1. Comparison of MUAP waveforms for plausibility checking

In our experimental measurements we included 8 female and 8 male healthy subjects with an age of $28.88 \pm 7.08$ years and normal BMI of $24.17 \pm 4.31$ kg/m$^2$. A total number of 167 MUs were identified across all 16 subjects and all 8 trials, which was less than in the anatomical model with 623 decomposed MUs.

For our plausibility check, a total of 52 and 299 MUAPs were evaluated for the experimental measurements and the anatomical muscle shape models, respectively. Although the statistical analysis revealed significant difference in $MUAP_{ptp_{max}}$ ($p < 0.001$) and $MUAP_{MNF_{max}}$ ($p < 0.001$) between experimentally obtained MUs and those from the mathematical model, boxplots in Fig. 4A showed overlapping value ranges. $MUAP_{MNF_{max}}$ was $66.65 \pm 16.72$ Hz for experimental measurements and $110.18 \pm 13.15$ Hz for the anatomical model. Differences for $MUAP_{ptp_{max}}$ were less pronounced with $0.77 \pm 0.74$ µV and $1.31 \pm 0.88$ µV, respectively.

The centered, normalized $MUAP_{ptp_n}$ and $MUAP_{MNF_n}$ maps are depicted in Fig. 4B. The experimental MUs were characterized by a noticeable attenuation of $MUAP_{ptp_n}$ toward the tendon ends. This was also evident in the anatomical model. In the medial–lateral direction, a broader PTP amplitude spread was observed in the experimental measurements than in the mathematical model. The map for $MUAP_{MNF_n}$ revealed a very similar pattern in the model with values in the range of the experimental measurement map.

Overall, the results showed that the anatomical model plausibly replicates the MUAP waveforms which provided a good basis for investigating muscle shape simplifications in a simulation study.

### 3.2. MU identification and validation in muscle shape simulations

Across 16 simulated random seeds, $346 \pm 46$ MUs were simulated in each muscle shape model, resulting in a total of 5536 MUs in our simulation study. Decomposition identified 623 MUs (anatomical), 728 MUs (fusiform), and 801 MUs (cylindrical) across all trials and seeds. For the anatomical model, the number of decomposed MUs per trial at 15%, 30%, 50% and 70% were $4.63 \pm 1.41$ MUs, $4.97 \pm 1.51$ MUs, $5.03 \pm 1.85$ MUs, and $4.84 \pm 1.75$ MUs, respectively (see Fig. 5A). Significant more MUs per trial were identified for both the simulations with the fusiform muscle shape ($p = 0.011, p = 0.009, p = 0.032, p = 0.004$) and those with the cylindrical muscle shape ($p = 0.002, p < 0.001, p = 0.007, p < 0.001$). The highest number of MUs, $6.69 \pm 1.67$ MUs, were identified for simulation trials at 70% MVCF with the cylindrical muscle shape.

The RoA between the identified MUs and the matched MUs of the simulations are presented in Fig. 5B. The highest average RoA of $97.30 \pm 7.37$ % was achieved for MUs identified from cylindrical muscle shape simulations at 50% MVCF and the lowest mean agreement of $94.63 \pm 12.16$ % was reached for MUs identified from anatomical simulations at 30% MVCF. No statistically significant differences ($p > 0.05$) were found with independent t-tests between the groups at any target force.

An illustration of identified MUs is shown in Fig. 5C. For all three muscle shape models, the majority of MUs were located in the anterior cross-sectional region in proximity to the electrodes. Only a few larger MUs located further away from the electrode grid were detected. The additionally decomposed MUs in the fusiform muscle and in the cylindrical muscle also accumulate primarily in the anterior region. Relative MU size was similar between the groups and no statistically significant differences ($p > 0.05$) were found (see Fig. 5D). An increasing trend of $MU_{size}$ was observable from 15% MVCF towards 70% MVCF for all three models.

## 4. Discussion

In this study, we investigated the performance of a blind source separation-based decomposition algorithm to identify MUs from simulations with different modeled muscle shapes. To this end, we implemented a volume conductor model with three levels of realism: an anatomical muscle geometry, a fusiform shape, and a simple cylindrical shape. For our evaluation, we simulated HDsEMG interference signals from 16 stochastic seeds during submaximal ramp contractions at four different target forces. Fiber positions, MU arrangements and myoelectrical properties were kept consistent across all models to ensure the maximum comparability.

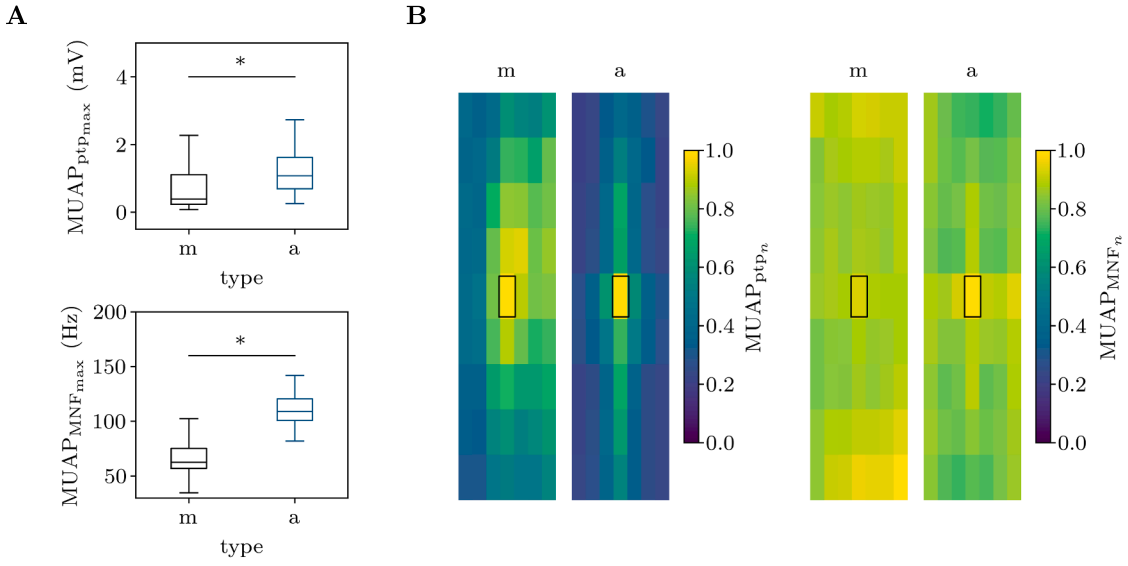


**Fig. 4.** Motor unit action potential (MUAP) waveform analysis: Panel A depicts boxplots with peak-to-peak amplitude ($MUAP_{ptp_{max}}$) and mean frequency ($MUAP_{MNF_{max}}$) of the MUAP channel with the highest peak-to-peak amplitude for experimental measurements (m) and anatomical muscle shape simulations (a). Differences between the measurements and muscle shape models which are statistically significant ($p < 0.05$) are marked with an asterisk (*). Normalized and centered metric maps ($MUAP_{ptp_n}$, $MUAP_{MNF_n}$) are presented in panel B.

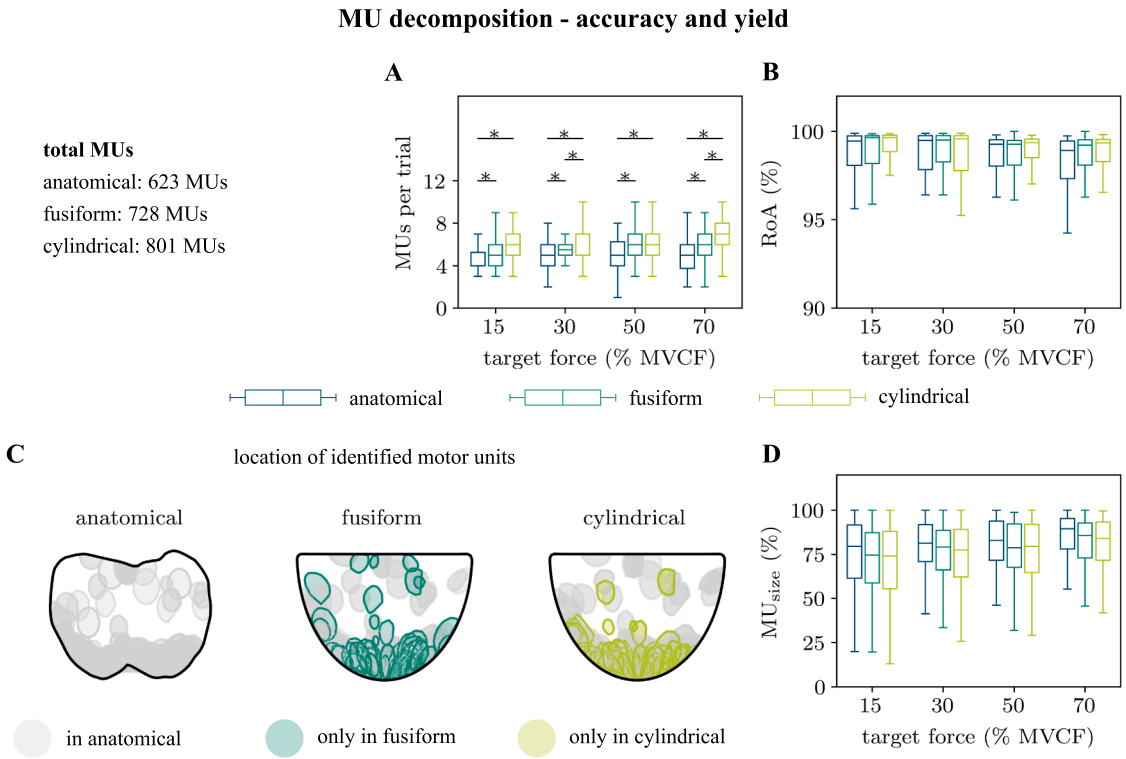


**Fig. 5.** Across all target forces 623 motor units (MUs), 728 MUs, and 801 MUs were identified with the anatomical (darkblue), fusiform (darkgreen) and cylindrical (lightgreen) muscle shape model, respectively. Panel A presents the number of identified MUs per simulation trial for each target force of the submaximal ramp contractions and muscle shape models, respectively. In all cases the cylindrical and fusiform model identified significantly more MUs per trial than the anatomical one ($p < 0.05$, marked with an asterisk *). Panel B evaluates the rate of agreement (RoA) between the identified MUs and matched ground-truth MUs. No significant differences were observed between models. The location of the identified MUs in the largest cross-section of the corresponding model are depicted in panel C. For all models the majority of MUs were positioned in the anterior part of the cross-section. MUs only identified by the fusiform or cylindrical muscle shape model are highlighted by darkgreen or lightgreen, respectively. The relative size of MUs is shown in panel D. MU sizes were comparable between muscle shape models with no statistically significant differences. MVCF: maximum voluntary contraction force.

MU decomposition based on HDsEMG recordings has become increasingly relevant over the past decade, as it enables extraction of representative MU properties that can only be roughly approximated from conventional sEMG features. By identifying MU discharge times, MU decomposition provides an estimate of the neural drive [Del Vecchio et al., 2020]. Newly developed algorithms not only endeavor to achieve a high accuracy in identifying MU discharge times, but also aim to maximize yield of detected MUs. The evaluation and validation of developed HDsEMG decomposition algorithms, however, remains an ongoing challenge. Experimentally, two-source validation approaches are used, in which both intramuscular and surface EMG are recorded simultaneously and evaluated using two independent algorithms. However, often only a small common portion of identified MUs is found. In this regard, modeling has become a valuable step in the development process [Farina et al., 2014].

Prior to our analysis, we verified the plausibility of the anatomical model with experimental measurement data. We observed qualitative agreement of spatiotemporal features, while $MUAP_{ptp_{max}}$ and $MUAP_{MNF_{max}}$ were higher in the model. Possible explanations include the use of a subject-independent volume conductor that ignores variability in subcutaneous tissue thickness and the numerous unknown physiological parameters that we estimated from cohort data in literature. Although the anatomical model exhibits quantitative differences compared to experimental data, it offers a known ground truth, thus, providing a solid foundation for our analysis.

Our simulation study regarding the decomposition performance revealed that significantly more MUs were identified with the fusiform and cylindrical models than with the anatomical one for all target forces of the submaximal ramp contractions (see Fig. 5A). The decomposed MUs had comparable MU sizes (see Fig. 5D) and were predominantly located in anterior regions (see Fig. 5C). Since myoelectric properties, relatively MU arrangements and firing instants were kept consistent across different models, these accumulations can mainly be attributed to the altered muscle geometries. The simplified shapes both caused smaller electrode-fiber distances in the muscle belly region and in case of the cylindrical shape also along the longitudinal muscle axis. Consequently, we hypothesize that less low-pass filtering was present, which increased signal-to-noise ratios of MUAPs and MU contributions in those regions, while the remaining muscle parts were comparable across geometries. Overall, this effect may lead to the higher yields.

To exploit the key advantage of simulations, which is the access to a known ground truth, we investigated the decomposition accuracy using the RoA between simulated and decomposed motor-unit spike trains. Across the simulated muscle shapes, RoA remained consistent with no statistically significant differences. In practice, this means that spike-train derived MU properties like firing frequencies or recruitment thresholds would be identified with equally high reliability across all muscle shape models. This outcome is consistent with the strong positive linear relationship between SIL and RoA reported by Negro et al., 2016. In our study, we retained MUs with SIL > 0.9. This stringent and recommended quality threshold is commonly used in the HDsEMG decomposition literature [Martinez-Valdes et al., 2023] and may indicate that regardless of the geometry only MUs with sufficiently distinct MUAP templates and strong contributions were included in the analysis. Taken together, the RoA-based timing accuracy for high-quality MUs remained stable across models, whereas differences between muscle

geometries manifested primarily as changes in yield.

Based on our evaluation of both decomposition yield and accuracy, we recommend using simulation models with anatomically derived volume conductors and realistic muscle shapes, which can be built using magnetic resonance scans. Our results showed that even small simplifications affecting fiber-electrode distances noticeably alter decomposition yield. These effects can be expected to be even stronger when highly simplified volume conductor models are used, which is frequently the case [Avrillon et al., 2024; Zhao et al., 2024]. Although we only conducted our evaluations on the biceps brachii, the results can most likely be directly applied to other muscles, where the fiber-electrode distances are changed due to simplifications. Consequently, comparison of decomposition algorithms validated with different simulation models should be viewed with caution.

The high level of complexity and the considerable implementation effort required remain obstacles to the broader application of anatomically derived sEMG models. Nevertheless, they provide valuable insight into signal characteristics and extend our physiological knowledge beyond the general signal characteristics captured by simplified analytical models [Farina et al., 2025]. Growth of computational power and new calculation methods will pave the way for subject-specific and dynamic models in the future [Ma et al., 2025; Maksymenko et al., 2023].

Three limitations of our study need to be acknowledged. Firstly, in this work a SIL $> 0.9$ was used as quality criterion for MU identification as recommended in Martinez-Valdes et al., 2023. Changes in SIL not only affect RoA [Negro et al, 2016], but may also affect the yield of the geometries. The threshold value should therefore be selected carefully according to the application. Secondly, manual editing of the MU discharge series may result in a bias which favors certain muscle shapes. While manual editing is generally associated with high inter-rater variability [Hug et al., 2021], we sought to minimize bias applying clear criteria with same amount of manual intervention across all geometries. In the future, a second rater and more automated decision rules would reduce the subjectivity of our results. Thirdly, we analyzed the influence of the simulated muscle shape only for a well-established decomposition algorithm based on blind source separation. Whether our recommendations extend to other classes of decomposition algorithms, i.e., algorithms based on machine learning techniques which are trained with simulation data, remains subject of further research. However, it could be hypothesized that models that are as accurate and subject specific as possible would also be advantageous in this case.

## 5. Conclusion

We have investigated the impact of the simulated muscle shape on HDsEMG decomposition yield and accuracy. All simulations were grounded in an anatomically derived biceps brachii model that plausibly reproduces MUAP waveforms, as verified against experimental HDsEMG. Our simulation study revealed that the modeled muscle shape significantly influenced the number of MUs identified with decomposition algorithms based on blind source separation, while the accuracy of identified MU discharge series remained consistent across muscle shapes. For a transparent assessment of decomposition algorithms, we suggest implementing simulation models that closely reflect anatomical reality since small deviations can lead to large differences in results. Nevertheless, systematic algorithm evaluation based on experimental data remains indispensable.

## Declaration of Generative AI and AI-assisted technologies in the writing process

During the preparation of this work the authors used Fraunhofer internal tool FhGenie [Weber et al., 2024] in order to improve language. After using this tool, the authors reviewed and edited the content as needed and take full responsibility for the content of the publication.

## CRediT authorship contribution statement

**Andra Oltmann:** Writing – review & editing, Writing – original draft, Visualization, Validation, Software, Methodology, Investigation, Data curation, Conceptualization. **Jan Graßhoff:** Writing – review & editing, Methodology, Conceptualization. **Tobias Knopp:** Writing – review & editing, Supervision, Conceptualization. **Philipp Rostalski:** Writing – review & editing, Supervision, Resources, Conceptualization.

## Declaration of competing interest

The authors declare that they have no known competing financial interests or personal relationships that could have appeared to influence the work reported in this paper.

## Acknowledgment

This work was funded by Land Schleswig-Holstein, Germany, Project: “Individualisierte Medizintechnik für bildgestützte, robotische Interventionen (IMTE2)”, Project No.: LPW21-L/2.2/262, 125 24 009.

## Appendix A. Supplementary data

Supplementary data to this article can be found online at https://doi.org/10.1016/j.jelekin.2025.103103.

## References

Armstrong, R.A., 2014. When to use the Bonferroni correction. Ophthalmic Physiol. Opt. 34 (5), 502–508. https://doi.org/10.1111/opo.12131.

Avrillon, S., Hug, F., Baker, S.N., Gibbs, C., Farina, D., 2024. Tutorial on MUedit: an open-source software for identifying and analysing the discharge timing of motor units from electromyographic signals. J. Electromyogr. Kinesiol. 77, 102886. https://doi.org/10.1016/j.jelekin.2024.102886.

Choi, H.F., Blemker, S.S., 2013. Skeletal muscle fascicle arrangements can be reconstructed using a Laplacian vector field simulation. PLoS One 8 (10), e77576. https://doi.org/10.1371/journal.pone.0077576.

Del Vecchio, A., Holobar, A., Falla, D., Felici, F., Enoka, R.M., Farina, D., 2020. Tutorial: Analysis of motor unit discharge characteristics from high-density surface EMG signals. J. Electromyogr. Kinesiol. 53, 102426. https://doi.org/10.1016/j.jelekin.2020.102426.

Duchateau, J., Enoka, R.M., 2022. Distribution of motor unit properties across human muscles. J. Appl. Physiol. 132 (1), 1–13. https://doi.org/10.1152/japplphysiol.00290.2021.

Farina, D., Holobar, A., 2016. Characterization of human motor units from surface EMG decomposition. Proc. IEEE 104 (2), 353–373. https://doi.org/10.1109/JPROC.2015.2498665.

Farina, D., Merletti, R., 2001. A novel approach for precise simulation of the EMG signal detected by surface electrodes. IEEE Trans. Biomed. Eng. 48 (6), 637–646. https://doi.org/10.1109/10.923782.

Farina, D., Merletti, R., Enoka, R.M., 2004a. The extraction of neural strategies from the surface EMG. J. Appl. Physiol. 96 (4), 1486–1495. https://doi.org/10.1152/japplphysiol.01070.2003.

Farina, D., Merletti, R., Enoka, R.M., 2014. The extraction of neural strategies from the surface EMG: an update. J. Appl. Physiol. 117 (11), 1215–1230. https://doi.org/10.1152/japplphysiol.00162.2014.

Farina, D., Merletti, R., Enoka, R.M., 2025. The extraction of neural strategies from the surface EMG: 2004-2024. J. Appl. Physiol. 138 (1), 121–135. https://doi.org/10.1152/japplphysiol.00453.2024.

Farina, D., Mesin, L., Martina, S., Merletti, R., 2004b. A surface EMG generation model with multilayer cylindrical description of the volume conductor. IEEE Trans. Biomed. Eng. 51 (3), 415–426. https://doi.org/10.1109/TBME.2003.820998.

Grison, A., Mendez Guerra, I., Clarke, A.K., Muceli, S., Ibáñez, J., Farina, D., 2025. Unlocking the full potential of high-density surface EMG: novel non-invasive high-yield motor unit decomposition. J. Physiol. 603 (8), 2281–2300. https://doi.org/10.1113/JP287913.

Hug, F., Avrillon, S., Del Vecchio, A., Casolo, A., Ibanez, J., Nuccio, S., et al., 2021. Analysis of motor unit spike trains estimated from high-density surface electromyography is highly reliable across operators. J. Electromyogr. Kinesiol. 58, 102548. https://doi.org/10.1016/j.jelekin.2021.102548.

Ma, S., Clarke, A.K., Maksymenko, K., Deslauriers-Gauthier, S., Sheng, X., Zhu, X., et al., 2025. Conditional generative models for simulation of EMG during naturalistic movements. IEEE Trans. Neural Networks Learn. Syst. 36 (5), 9224–9237. https://doi.org/10.1109/TNNLS.2024.3438368.

Maksymenko, K., Clarke, A.K., Mendez Guerra, I., Deslauriers-Gauthier, S., Farina, D., 2023. A myoelectric digital twin for fast and realistic modelling in deep learning. Nat. Commun. 14, 1600. https://doi.org/10.1038/s41467-023-37238-w.

Martinez-Valdes, E., Enoka, R.M., Holobar, A., McGill, K., Farina, D., Besomi, M., et al., 2023. Consensus for experimental design in electromyography (CEDE) project: Single motor unit matrix. J. Electromyogr. Kinesiol. 68, 102726. https://doi.org/10.1016/j.jelekin.2022.102726.

Mendez Guerra, I., Barsakcioglu, D.Y., Farina, D., 2024. Adaptive EMG decomposition in dynamic conditions based on online learning metrics with tunable hyperparameters. J. Neural Eng. 21 (4). https://doi.org/10.1088/1741-2552/ad5ebf.

Merletti, R., Farina, D., 2016. Surface Electromyography: Physiology, Engineering, and applications. John Wiley & Sons, Inc, Hoboken, New Jersey.

Mitsuhashi, N., Fujieda, K., Tamura, T., Kawamoto, S., Takagi, T., Okubo, K., 2009. BodyParts3D: 3D structure database for anatomical concepts. Nucleic Acids Res. 37, D782–D785. https://doi.org/10.1093/nar/gkn613.

Negro, F., Muceli, S., Castronovo, A.M., Holobar, A., Farina, D., 2016. Multi-channel intramuscular and surface EMG decomposition by convolutive blind source separation. J. Neural Eng. 13 (2), 026027. https://doi.org/10.1088/1741-2560/13/2/026027.

Pereira Botelho, D., Curran, K., Lowery, M.M., 2019. Anatomically accurate model of EMG during index finger flexion and abduction derived from diffusion tensor imaging. PLoS Comput. Biol. 15 (8), e1007267. https://doi.org/10.1371/journal.pcbi.1007267.

Petersen, E., Rostalski, P., 2019. A comprehensive mathematical model of motor unit pool organization, surface electromyography, and force generation. Front. Physiol. 10, 176. https://doi.org/10.3389/fphys.2019.00176.

Villani, C., 2008. Optimal Transport: Old and New. Springer, Berlin, Heidelberg.

Weber, I., Linka, H., Mertens, D., Muryshkin, T., Opgenoorth, H., Langer, S., 2024. FhGenie: A Custom, Confidentiality-Preserving Chat AI for corporate and Scientific Use. 2024 IEEE 21st International Conference on Software Architecture Companion (ICSA-c). IEEE.

Zhao, H., Zhang, X., Chen, M., Zhou, P., 2024. Adaptive online decomposition of surface EMG using progressive FastICA peel-off. IEEE Trans. Biomed. Eng. 71 (4), 1257–1268. https://doi.org/10.1109/TBME.2023.3331498.